A&A 536, A105 (2011)
DOI: 10.1051/0004-6361/201117752

Astronomy & Astrophysics

X-shooter, the new wide band intermediate resolution spectrograph at the ESO Very Large Telescope

J. Vernet[1], H. Dekker[1], S. D'Odorico[1], L. Kaper[2], P. Kjaergaard[3], F. Hammer[4], S. Randich[5], F. Zerbi[6], P. J. Groot[7], J. Hjorth[3], I. Guinouard[4], R. Navarro[8], T. Adolfse[7], P. W. Albers[7], J.-P. Amans[4], J. J. Andersen[3], M. I. Andersen[3], P. Binetruy[9], P. Bristow[1], R. Castillo[10], F. Chemla[4], L. Christensen[11], P. Conconi[6], R. Conzelmann[1], J. Dam[7], V. De Caprio[12], A. De Ugarte Postigo[3], B. Delabre[1], P. Di Marcantonio[13], M. Downing[1], E. Elswijk[8], G. Finger[1], G. Fischer[1], H. Flores[4], P. François[4], P. Goldoni[9], L. Guglielmi[9], R. Haigron[4], H. Hanenburg[8], I. Hendriks[7], M. Horrobin[14], D. Horville[4], N. C. Jessen[15], F. Kerber[1], L. Kern[1], M. Kiekebusch[1], P. Kleszcz[8], J. Klougart[3], J. Kragt[8], H. H. Larsen[3], J.-L. Lizon[1], C. Lucuix[1], V. Mainieri[1], R. Manuputy[16], C. Martayan[10], E. Mason[17], R. Mazzoleni[6], N. Michaelsen[3], A. Modigliani[1], S. Moehler[1], P. Møller[1], A. Norup Sørensen[3], P. Nørregaard[3], C. Péroux[18], F. Patat[1], E. Pena[10], J. Pragt[8], C. Reinero[10], F. Rigal[8], M. Riva[6], R. Roelfsema[8], F. Royer[4], G. Sacco[19], P. Santin[13], T. Schoenmaker[8], P. Spano[6], E. Sweers[7], R. Ter Horst[8], M. Tintori[20], N. Tromp[8], P. van Dael[7], H. van der Vliet[7], L. Venema[8], M. Vidali[21], J. Vinther[1], P. Vola[18], R. Winters[7], D. Wistisen[3], G. Wulterkens[7], and A. Zacchei[13]

(Affiliations can be found after the references)

Received 21 July 2011 / Accepted 27 September 2011

ABSTRACT

X-shooter is the first 2nd generation instrument of the ESO Very Large Telescope (VLT). It is a very efficient, single-target, intermediate-resolution spectrograph that was installed at the Cassegrain focus of UT2 in 2009. The instrument covers, in a single exposure, the spectral range from 300 to 2500 nm. It is designed to maximize the sensitivity in this spectral range through dichroic splitting in three arms with optimized optics, coatings, dispersive elements and detectors. It operates at intermediate spectral resolution ($R \sim 4000-17\,000$, depending on wavelength and slit width) with fixed échelle spectral format (prism cross-dispersers) in the three arms. It includes a $1.8'' \times 4''$ integral field unit as an alternative to the $11''$ long slits. A dedicated data reduction package delivers fully calibrated two-dimensional and extracted spectra over the full wavelength range. We describe the main characteristics of the instrument and present its performance as measured during commissioning, science verification and the first months of science operations.

Key words. instrumentation: spectrographs

1. Introduction

On November 19, 2001, the European Southern Observatory (ESO) issued a call for proposals for 2nd generation VLT instruments. Four instrument concepts were quoted in the call as being of particular interest to the ESO community: a cryogenic multi-object spectrometer in the 1 to 2.4 μm range, a wide-field 3D optical spectrometer, a high contrast, adaptive optics assisted, imager (Planet Finder) and a medium resolution, wide-band (0.32–2.4 μm) spectrometer. In 2002 four proposals were received on this latter instrument concept. Following a phase of discussions between the various proponents and ESO, a consortium was formed between ESO and several partner institutes in Denmark, France, Italy and the Netherlands to carry out a feasibility study. After interaction with the ESO Scientific and Technical Committee (STC), the study was presented in final form to ESO in October 2003 and the project was finally approved by the ESO Council in December 2003 (D'Odorico et al. 2004, 2006).

After a preliminary design review in 2004 and a final design review in 2006, the different hard- and software components of the instrument were manufactured, integrated and tested at the 10 consortium institutes (Table 1). Final integration of the full instrument was done at ESO headquarters in Garching, Germany, before it was installed and commissioned on the VLT at ESO Paranal, Chile (Vernet et al. 2009). The instrument was completed in 5 years (along with the near-IR camera HAWK-I, the shortest construction time of VLT instruments so far) at a cost of about 5.3 million Euro and about 70 person-years. The major fraction of the hardware costs and manpower were provided by the consortium institutes, and compensated by ESO with guaranteed time observations (GTO) on the VLT. The X-shooter GTO program includes about 150 nights and is being executed in a three-year period (2009–2012).

The X-shooter project was led by a project board consisting of four national principal investigators (PIs) and the ESO PI (see Table 1) and met about once every six months. Sadly, the Italian co-PI R. Pallavicini passed away on January 10, 2009. The overall project management and system engineering was in hands of H. Dekker (ESO), assisted by F. Zerbi (ESO). The X-shooter Science Team was led by J. Hjorth (DK) and subsequently P. J. Groot (NL). J. Vernet (ESO) has been appointed as the X-shooter Instrument Scientist. Activities within each country were coordinated by a national project manager (PM); the work package managers reported to their national PM who had a monthly teleconference with the other PMs and H. Dekker.

The concept of X-shooter has been defined with one principle goal in mind: the highest possible throughput over the wavelength range from the atmospheric cutoff to the near infrared at a resolution where the instrument is sky limited in a half hour exposure. Sky background and detector noise considerations

Table 1. An overview of the hardware and software contributions to X-shooter from the different consortium partners.

ESO	PI S. D'Odorico, PM H. Dekker
	Detector systems Flexure compensation system Cryogenic control electronics Data reduction software Final integration and commissioning
Denmark	PI and PM P. Kjaergaard Rasmussen
Niels Bohr Institute, Copenhagen University, DTU Space, Copenhagen	UVB & VIS spectrograph (mechanics) Instrument backbone Pre-slit optics and calibration system Instrument control electronics
France	PI F. Hammer, PM I. Guinouard
Paris Observatory Meudon Astroparticle and Cosmology Paris	Integral field unit Data reduction software
Italy	PI R. Pallavicini/S. Randich, PM F. Zerbi
INAF Observatory Palermo, INAF Observatory Brera, INAF Observatory Trieste, INAF Observatory Catania	UVB & VIS spectrographs (optics) Instrument Control Software
The Netherlands	PI L. Kaper, PM R. Navarro
Netherlands Research School for Astronomy (NOVA) Astronomical Institute, University of Amsterdam Astronomical Institute, Radboud University Nijmegen ASTRON Dwingeloo	NIR spectrograph NIR cryostat Data reduction software

require that the spectral resolution is in the range 5000 to 7000 (for a 1″ slit). This resolution also ensures that in the near infrared, 80 to 90% of the detector pixels are not affected by strong sky lines so that most of the covered spectrum is sky background continuum limited. Other constraints on the design of X-shooter were set by the size and weight (and related flexure) limits of the VLT Cassegrain focus.

The X-shooter science case (see ESO/STC-324A) is broad and includes various applications ranging from nearby intrinsically faint stars to bright sources at the edge of the Universe. X-shooter's unique wavelength coverage and high efficiency opens a new observing capacity in observational astronomy. Key science cases to be addressed with X-shooter concern the study of brown dwarfs, young stellar objects and T Tauri stars, the progenitors of supernovae type Ia, gamma-ray bursts (GRB), quasar absorption lines, and lensed high-z galaxies. The advantage of the large wavelength coverage is that e.g. the redshift of the target does not need to be known in advance (as is the case for GRBs); also, the study of Lyman α in high-redshift galaxies will be possible in the redshift range $1.5 < z < 15$. VLT/X-shooter will complement and benefit from other major facilities in observational astrophysics operational in the period 2010–2020: survey instruments like VST/OmegaCAM and VISTA working in the same wavelength range, and observatories like LOFAR, ALMA, JWST, *Swift* and *Fermi* exploring other observing windows.

An overview of the instrument design is given in Sect. 2. Performance (resolution, throughput, background, stability) as measured during testing, commissioning and the first months of science operations is discussed in Sect. 3. In Sect. 4 we summarize the conclusions and provide some suggestions for improvement of the instrument performance. We conclude in Sect. 5 with an example of a quasar observation obtained during commissioning as an illustration of the unique capabilities of the instrument.

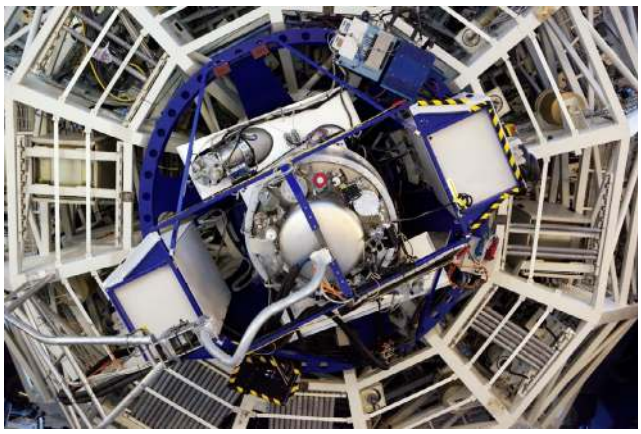

Fig. 1. A view of X-shooter at the Cassegrain focus below the primary mirror cell of the VLT UT2. In this view from below the instrument one sees the UVB and VIS spectrographs at the top and bottom, respectively. The NIR cryostat is visible in the center. The two boxes on the left and on the right are electronic cabinets.

2. Instrument design

X-shooter consists of a central structure (the backbone) that supports three prism-cross-dispersed échelle spectrographs optimized for the UV-blue (UVB), visible (VIS) and near-IR (NIR) wavelength ranges, respectively. After the telescope focus, a series of two highly efficient dichroics reflect the UVB and VIS light to the corresponding arms and transmit longer wavelengths to the NIR arm. A slicer can be inserted in the focal plane, which reformats 1.8″ × 4″ on the sky into a 0.6″ × 12″ long slit. A slit unit equipped with 11″ long slits of different widths is located at the entrance of each spectrograph. A functional diagram of the instrument is given in Fig. 2.

In this section, we give an overview of the design of X-shooter following photons coming from the telescope.

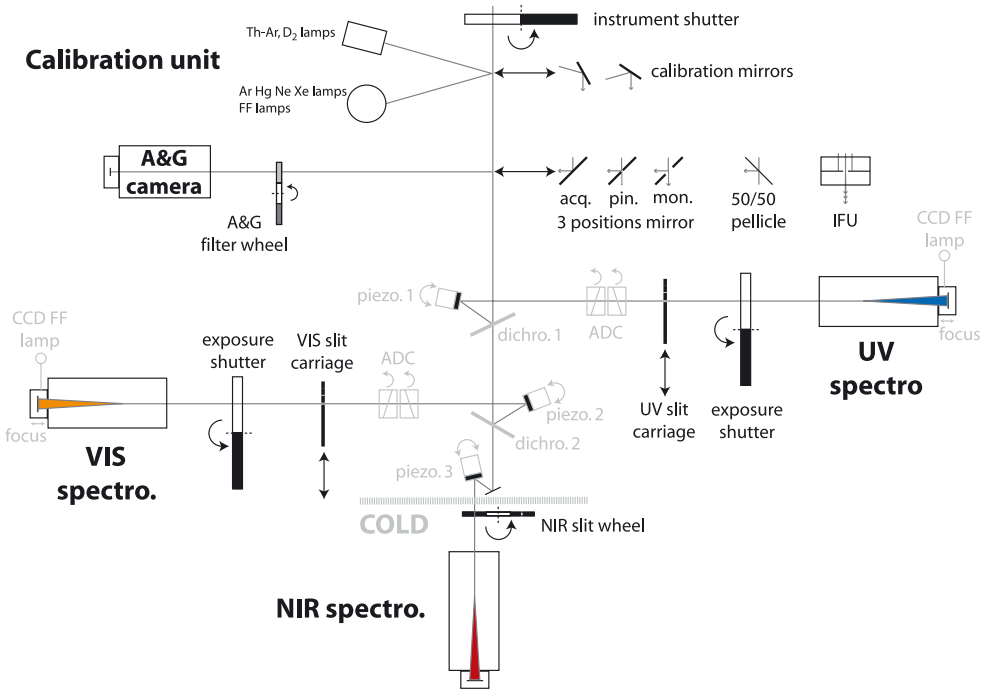

Fig. 2. Functional diagram of X-shooter. The light path runs from the top to the bottom of the figure. Each element is described in Sect. 2.

For more detailed discussions of specific aspects and the manufacturing process please refer to the following publications: Spanò et al. (2006) for the optical design; Rasmussen et al. (2008) for the backbone and the UVB and VIS spectrographs; Navarro et al. (2006, 2008) for the NIR spectrograph; Roelfsema et al. (2008) for the cryogenic design; Guinouard et al. (2006) for the Integral Field Unit; Vidali et al. (2006) for the control software; Goldoni et al. (2006) and Modigliani et al. (2010) for the data reduction software.

2.1. Key design choices

A number of key design choices were made in the phases of the project definition. Possibly the most crucial design choice was on the method used to split the incoming beam from the telescope between the three spectral arms. The option to use a single slit in the telescope focal plane was rejected because of the difficulty of designing a highly efficient relay system and atmospheric dispersion correction for the full spectral range, and the need for work-packages with clean interfaces to be handled by the different consortium partners, which is not possible when spectrographs are sharing a single slit. The solution that was finally adopted is based on the sequential use of two dichroics after the focal plane, used at 15° rather than 45° to minimize polarization effects. The beams toward the UVB and VIS spectrographs are then deviated to 90° with folding mirrors. These two folding mirrors together with one in the NIR path are actively controlled to compensate for small motions due to flexures in the backbone of the instrument and guarantee that the three target images all remain centered on the three slit units as the telescope is tracking (see Sect. 3.5.2).

The optical design allows the introduction of two short-wavelength atmospheric dispersion correctors (ADC) and the focusing of the target on the slit units at the entrance of the respective arms.

The size, weight and flexure restrictions implied a very compact optical design of the spectrographs, requiring an efficient folding of the light path, especially for the NIR-arm. The solution was found in selecting the "4C" design described in Delabre et al. (1989).

The inclusion of the K-band was the subject of a complex trade-off. With its uncooled optics in the pre-slit area the instrument could not be optimized for a low thermal background. On the other hand the K-band did fit well in the spectral format on the detector and had a potentially high efficiency. It was finally decided to include the band, but its inclusion should not reduce the performance in the J- and H-bands. It was also decided not to cool the instrument pre-slit optics.

Another key design choice was the spectral resolution in the three arms. The goal was to build an instrument which reaches the dark sky noise limit in about 30 min, while still providing medium resolution to do quantitative work on emission and absorption lines. In the NIR the resolution of 5600 for 0.9″ slit permits the full separation (and subtraction) of the sky emission lines. At UVB and VIS wavelengths, specific scientific programs did call for higher resolving power, e.g. to optimally measure abundances. The final choices (see Table 4) are obviously a compromise to cover a broad range of astrophysical programs.

2.2. The backbone

2.2.1. The instrument shutter and the calibration unit

In the converging beam coming from the telescope, the first element is the telescope entrance shutter which allows safe daytime use of X-shooter for tests and calibration without stray-light entering the system from the telescope side.

This is followed by the calibration unit that allows selection from a set of flat-fielding and wavelength calibration lamps carefully chosen to cover the whole wavelength range (Saitta et al. 2008; Kerber et al. 2008). This unit consists of a mechanical structure holding calibration lamps, an integrating sphere, relay optics that simulate the $f/13.6$ telescope beam, and a mirror slide with 3 positions that can be inserted in the telescope beam:

- one free position for a direct feed from the telescope;

- one mirror that reflects the light from the integrating sphere equipped with:
  - wavelength calibration Ar, Hg, Ne and Xe Penray lamps operating simultaneously;
  - three flat-field halogen lamps equipped with different balancing filters to optimize the spectral energy distribution for each arm;
- one mirror which reflects light from:
  - a wavelength calibration hollow cathode Th-Ar lamp;
  - a D_2 lamp for flat-fielding the bluest part of the UVB spectral range.

2.2.2. The acquisition and guiding slide

Light coming either directly from the telescope or from the calibration unit described above arrives at the acquisition and guiding slide (hereafter A&G slide). This structure allows the insertion into the beam of one of the following components:

- a flat 45° mirror with three positions for:
  - acquisition and imaging (labeled ACQ. in Fig. 2): the full $1.5' \times 1.5'$ field of view is sent to the A&G camera. This is the position used during all acquisition sequences;
  - spectroscopic observations and monitoring (labeled MON. in Fig. 2): a slot lets the central $10'' \times 15''$ of the field go through to the spectrographs while reflecting the peripheral field to the A&G camera. This is the position used for all science observations;
  - optical alignment and engineering purposes: a 0.5″ pinhole producing an artificial star (labeled PIN. in Fig. 2) is placed in the focal plane;
- the integral field unit (IFU, see Sect. 2.2.3);
- a 50/50 pellicle beam splitter at 45° used to look down into the instrument with the A&G camera for engineering purposes.

2.2.3. The IFU

The integral field unit is an image slicer that re-images an input field of $4'' \times 1.8''$ into a pseudo slit of $12'' \times 0.6''$. The light from the central slice is directly transmitted to the spectrographs. The two lateral sliced fields are reflected toward the two pairs of spherical mirrors and re-aligned at both ends of the central slice in order to form the exit slit as illustrated in Fig. 3. Due to these four reflections the throughput of the two lateral fields is reduced with respect to the directly transmitted central one. The measured overall efficiency of the two lateral slitlets is 85% of the direct transmission but drops to 50% below 400 nm due to reduced coating efficiency in the blue. Note that each spectrograph is equipped with a dedicated $12.6'' \times 1''$ opening to be used in combination with the IFU. It is slightly larger than the IFU pseudo slit ensuring that the whole field of view is transmitted while baffling ghosts.

2.2.4. The acquisition and guiding camera

The A&G camera allows visual detection and centerering of objects from the U- to the z-band. This unit consists of:

- a filter wheel equipped with a full UBVRI Johnson filter set and a full Sloan Digital Sky Survey (SDDS) filter set;
- a Peltier cooled, 13 μm pixel, 512×512 E2V broad band coated Technical CCD57−10 onto which the focal plane is re-imaged at $f/1.91$ through a focal reducer. This setup provides a plate scale of 0.173″/pix and a field of view of $1.47' \times 1.47'$.

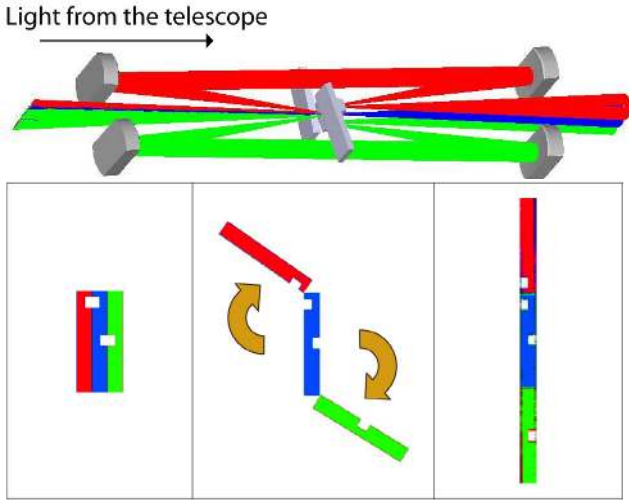

Fig. 3. *Top*: view of the effect of the IFU. The central field is directly transmitted to form the central slitlet (blue) while each lateral field (in red and green) is reflected toward a pair of spherical mirrors, and re-aligned at the end of the central slice to form the exit slit. *Bottom*: the field before (*left*) and after the IFU (*right*). The IFU acts such that the lateral fields are rotated. The two white slots are not real gaps but just guides to help visualize the top and the bottom of each slice in the drawing.

This acquisition device – that can also be used to record images of the target field through different filters – provides a good enough sampling to measure the centroid of a target to better than 0.1″ accuracy in all seeing conditions.

2.2.5. The dichroic box

Light is split and distributed to the three arms by two highly efficient dichroic beam splitters. These are the first optical elements encountered by the science light (unless the IFU is deployed). The first dichroic at an incidence angle of 15° reflects more than 98% of the light between 350 and 543 nm and transmits ∼95% of the light between 600 and 2300 nm. The second dichroic, also at 15° incidence, has a reflectivity above 98% between 535 nm and 985 nm and transmits more than 96% of the light between 1045 and 2300 nm. The combined efficiency of the two dichroics is shown in Fig. 4: it is well above 90% over most of the spectral range.

2.2.6. The flexure compensation tip-tilt mirrors

Light reflected and/or transmitted by the two dichroics reaches, in each arm, a folding mirror mounted on a piezo tip-tilt mount (S-340 from Physik Instrumente). These mirrors are used to fold the beam and correct for backbone flexure to keep the relative alignment of the three spectrograph slits fixed at any orientation of the telescope and instrument. Operational aspects and performance of the flexure compensation system are addressed in Sect. 3.5.2.

For slit observations (but not IFU) these tip-tilt mirrors also compensate for shifts due to atmospheric differential refraction between the telescope tracking wavelength (fixed at 470 nm) and the undeviated wavelength of the two atmospheric dispersion

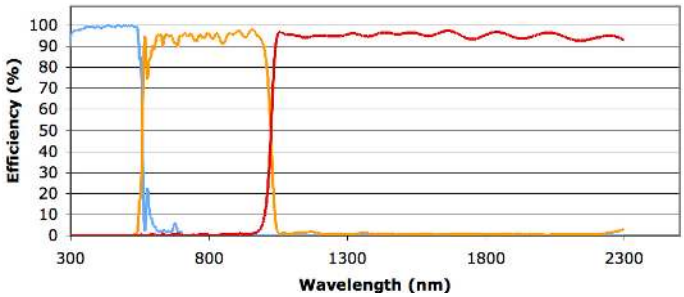

Fig. 4. The combined efficiency of the two dichroic beam splitters. In blue: reflection on the first dichroic; in orange: transmission through the first dichroic and reflection on the second dichroic; in red: transmission through both dichroics.

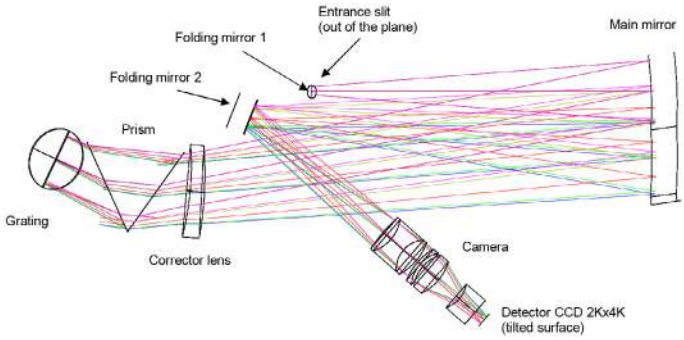

Fig. 5. The UVB spectrograph optical layout. The optical layout of the VIS spectrograph is very similar to this one.

correctors (for UVB and VIS arms, see Sect. 2.2.7) and the middle of the atmospheric dispersion range for the NIR arm.

2.2.7. The focal reducer and atmospheric dispersion correctors

Both UVB and VIS pre-slit arms contain a focal reducer and an atmospheric dispersion corrector (ADC). These focal reducer-ADCs consist of two doublets cemented onto two counter rotating double prisms. The focal reducers bring the focal ratio from $f/13.41$ to $f/6.5$ and provide a measured plate scale at the entrance slit of the spectrographs of 3.91″/mm in the UVB and 3.82″/mm in the VIS. The ADCs compensate for atmospheric dispersion in order to minimize slit losses and allow orienting the slit to any position angle on the sky up to a zenith distance of 60°. The zero deviation wavelengths are 405 and 633 nm for the UVB and the VIS ADCs, respectively. During slit observations, their positions are updated every 60 s based on information taken from the telescope database.

Since the IFU comes ahead of the ADCs in the optical train, no correction for atmospheric dispersion is available for IFU observations, and the ADCs are set to their neutral position in this observing mode.

The NIR arm is not equipped with an ADC. The NIR arm tip-tilt mirror compensates for atmospheric refraction between the telescope tracking wavelength (470 nm) and 1310 nm which corresponds to the middle of the atmospheric dispersion range for the NIR arm. This means that this wavelength is kept at the center of the NIR slit. At a zenith distance of 60° the length of the spectrum dispersed by the atmosphere is 0.35″, so the extremes of the spectrum can be displaced with respect to the center of the slit by up to 0.175″.

2.3. The UVB spectrograph

2.3.1. Slit carriage

The first opto-mechanical element of the spectrograph is the slit carriage. Besides the slit selection mechanism, this unit consists of a field lens placed just in front of the slit to re-image the telescope pupil onto the spectrograph grating, and the spectrograph shutter just after the slit. The slit mask is a laser cut Invar plate manufactured with a LPKF Laser Cutter. It is mounted on a motorized slide in order to select one of the 9 positions available. All science observation slits are 11″ high and different widths are available: 0.5″, 0.8″, 1.0″, 1.3″, 1.6″ and 5″ (the latter for spectro-photometric calibration, see Table 4). In addition a single pinhole for spectral format check and order tracing and a 9-pinhole mask for wavelength calibration and spatial scale mapping are available. A 12.6″ × 1″ slit is also available to be used in combination with the IFU (see Sect. 2.2.3).

2.3.2. Optical layout

The optical layout of the UVB spectrograph is presented in Fig. 5. Light from the entrance slit, placed behind the plane of the figure, feeds a 5° off-axis Maksutov-type collimator through a folding mirror. The collimator consists of a spherical mirror and a diverging fused silica (SiO_2) corrector lens with only spherical surfaces. The collimated beam passes through a 60° silica prism twice to gain enough cross-dispersion. The main dispersion is achieved through a 180 grooves/mm échelle grating blazed at 41.77°. The off-blaze angle is 0.0°, while the off-plane angle is 2.2°. After dispersion, the collimator creates an intermediate spectrum near the entrance slit, where a second folding mirror has been placed. This folding mirror acts also as a field mirror. Then a dioptric camera (4 lens groups with CaF_2 or silica lenses, one aspherical surface) re-images the cross-dispersed spectrum at $f/2.7$ (plate scale 9.31″/mm) onto a detector that is slightly tilted to compensate for a variation of best focus with wavelength. The back focal length is rather sensitive to temperature changes. It varies by ∼22.7 μm/°C which corresponds to a defocus of 9 μm/°C or ∼0.08″/°C. This is automatically compensated for at the beginning of every exposure by moving the triplet+doublet of the camera by −10.9 μm/°C.

2.3.3. Detector

The UVB detector is a 2048 × 4102, 15 μm pixel CCD from E2V (type CCD44-82) of which only a 1800 × 3000 pixels window is used. The CCD cryostat is attached to the camera with the last optical element acting as a window. The operating temperature is 153 K. The CCD control system is a standard ESO FIERA controller (see Beletic et al. 1998) shared with the VIS CCD. The associated shutter, located just after the slit, is a 25 mm bi-stable shutter from Uniblitz (type BDS 25). Full transit time is 13 ms. Since the slit is 2.8 mm high (11″ at $f/6.5$), the illumination of the detector is homogeneous to within ≪10 ms.

2.4. The VIS spectrograph

2.4.1. Slit carriage

The slit carriage of the VIS spectrograph is identical to that of the UVB arm (see Sect. 2.3.1), but the available slits are different.

All the science observation slits are 11″ high and the slit widths are: 0.4″, 0.7″, 0.9″, 1.2″, 1.5″ and 5″ (see Table 4).

2.4.2. Optical layout

The optical layout of the VIS spectrograph is very similar to that of the UVB (see Fig. 5). The collimator (mirror+corrector lens) is identical. For cross-dispersion, it uses a 49° Schott SF6 prism in double pass. The main dispersion is achieved through a 99.4 grooves/mm, 54.0° blaze échelle grating. The off-blaze angle is 0.0° and the off-plane angle is 2.0°. The camera (three lens groups, one aspherical surface) re-images the cross-dispersed spectrum at $f/2.8$ (plate scale 8.98″/mm) onto the detector (not tilted). Focussing is obtained by acting on the triplet+doublet sub-unit of the camera. However, unlike the UVB arm, the back focal length varies by less than 1 μm/°C (image blur <0.004″/°C) hence no thermal focus compensation is needed.

2.4.3. Detector

The VIS detector is a 2048 × 4096, 15 μm pixel CCD from MIT/LL (type CCID-20). As in the UVB arm, the cryostat is attached to the camera with the last optical element acting as a window. The operating temperature is 135 K. It shares its controller with the UVB detector. The associated shutter system is identical to the UVB one.

2.5. The NIR spectrograph

The NIR spectrograph is fully cryogenic. It is cooled with a liquid nitrogen bath cryostat and operates at 105 K.

2.5.1. Pre-slit optics and entrance window

After the dichroic box and two warm mirrors M1 (cylindrical) and M2 (spherical), mounted on a tip-tilt stage and used for flexure compensation (see Sect. 2.2.6), light enters the cryostat via the Infrasil vacuum window. To avoid ghosts, this window is tilted by 3°. After the window, light passes the cold stop, and is directed towards the slit via two folding mirrors M3 (flat) and M4 (spherical).

2.5.2. Slit wheel

A circular laser cut Invar slit mask is pressed in between two stainless steel disks with 12 openings forming the wheel. The wheel is positioned by indents on the circumference of the wheel with a roll clicking into the indents. All the science observation slits are 11″ high and different widths are offered: 0.4″, 0.6″, 0.9″, 1.2″, 1.5″ and 5″ (see Table 4). As for the two other arms, a single pinhole, a 9 pinhole mask and an IFU dedicated 12.6″ × 1″ slit are available.

2.5.3. Optical layout

The optical layout of the NIR spectrograph is presented in Fig. 6. The conceptual design is the same as for the UVB and the VIS spectrographs. Light entering the spectrograph via the entrance slit and folding mirror M5 feeds an off-axis Maksutov-inspired collimator. In this case, the collimator is made of two spherical mirrors M6 and M7 plus an Infrasil corrector lens (with only spherical surfaces). In order to get enough cross dispersion, three prisms are used in double pass. Prism 1 is a 35° top angle made

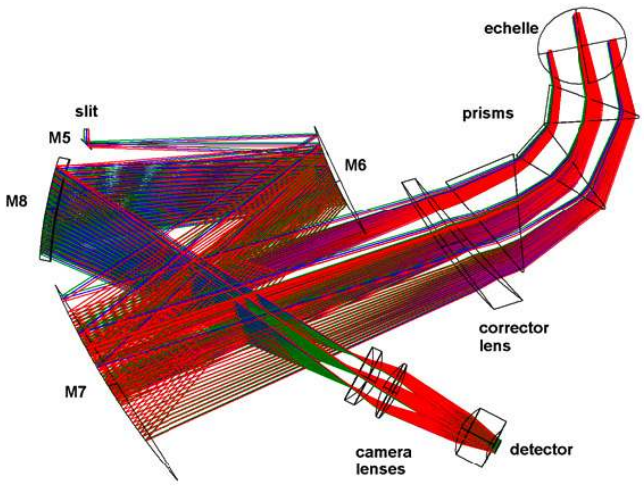

Fig. 6. The NIR spectrograph optical layout.

of Infrasil; prisms 2 and 3 are two 22° top angle ZnSe prisms of the largest available thickness (56 mm). This design provides an almost constant order separation. The main dispersion is provided by a 55 grooves/mm échelle grating with a blaze angle of 46.07°. The off-blaze angle is 0.0°, while the off-plane angle is 1.8°. After dispersion, the collimator creates an intermediate spectrum near the entrance slit, where M8, a spherical mirror, acts as a field mirror, relocating the pupil between L2 and L3, the last lenses of the camera. The fixed focus camera re-images the échellogram onto the detector at $f/2.1$ (plate scale 12.1″/mm).

The optical box and the mechanical structures of the optical elements are made out of a single block of aluminum, designed such that after cooling down the optical elements are accurately positioned taking into account the shrinkage of the aluminum. To reduce flexure, extreme lightening techniques have been applied to reduce the weight of the NIR spectrograph at the bottom of the instrument in the Cassegrain focus.

2.5.4. Detector

The NIR detector is a Teledyne substrate-removed HgCdTe, 2k × 2k, 18 μm pixel Hawaii 2RG of which only 1k × 2k is used. It is operated at 81 K. Cooling is achieved through a heat link (a massive 40 mm × 40 mm copper bar) plunged directly into the bottom of the liquid N_2 tank. The array control system is the ESO standard IRACE controller (Meyer et al. 1998). Sample-up-the-ramp (non-destructive) readout is always used. This means that during integration, the detector is continuously read out without resetting it and counts in each pixel are computed by fitting the slope of the signal vs. time. In addition, threshold limited integration (TLI) mode is used to extend the dynamical range for long exposure times: if one pixel is illuminated by a bright source and reaches an absolute value above a certain threshold (close to detector saturation), only detector readouts before the threshold is reached are used to compute the slope and the counts written in the FITS image for this pixel are extrapolated to the entire exposure time (see Finger et al. 2008).

To significantly decrease persistence, a global reset is applied immediately after finishing science exposures and pixels of the array are kept at the reset voltage until the next exposure starts. The release of trapped charge during a dark exposure immediately following an exposure to a bright light source is the cause of the persistence effect. If all pixels of the array are con-

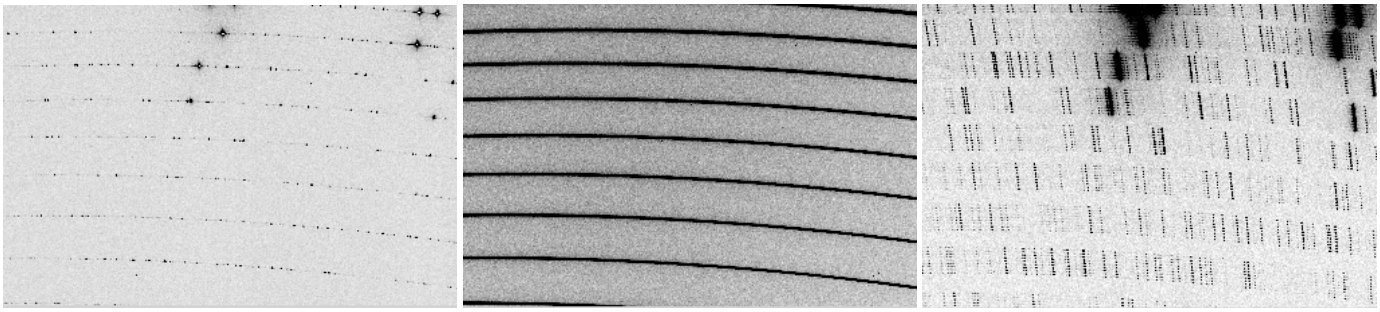

Fig. 7. Sections (1365 pix × 925 pix) of VIS arm calibration frames used by the data reduction pipeline to fully characterize the spectral format. From left to right: a single pinhole arc frame ("format check"), a single pinhole continuum frame ("order definition") and a 9-pinhole arc frame used for spatial scale and wavelength calibration.

nected to the reset voltage the diode junctions and the width of their depletion regions do not change even if the array is exposed to a bright light source with photons generating charge. Hence, no traps in the depletion region are exposed to majority carriers. On the contrary, trapped charge is released during the global reset before the next exposure starts. By two minutes of global reset de-trapping (typical time interval in between two science exposures in a nodding sequence) the persistence effect can be reduced by a factor of ten. If the reset switch is kept closed during the bright exposure prior to the dark exposures the persistence is eliminated and the global reset acts like an electronic shutter protecting the detector from exposure to bright sources.

2.6. The instrument control and observing software

The X-shooter control software is based on the standard ESO VLT control software (see Raffi & Wirenstrand 1997). The number of functions to control is relatively low compared to other large VLT instruments (8 calibration lamps; 13 motors; 3 tip-tilt piezoelectric actuators; 55 digital and analog sensors and 4 detectors, see Fig. 2). The two most critical aspects are: the synchronization of exposures between the three arms and the real time flexure compensation, see Sect. 3.5.2.

2.7. Data reduction software

Delivery of the X-shooter data reduction pipeline[1] (Goldoni et al. 2006; Modigliani et al. 2010) was an important part of the X-shooter project. It provides recipes for Paranal science operations, for data quality control at ESO headquarters and for offline data reduction by science users. While it is used in a fully automated mode for quick-look data evaluation on Paranal, the pipeline is fully configurable through an extended set of parameters to allow astronomers to tune the reduction to their specific needs. Pipeline recipes can be executed either with the ESO recipe execution tool (EsoRex[2]) at the command line level or through the Gasgano[3] graphical user interface. The recipes are implemented with the ESO Common Pipeline Library (CPL, Banse et al. 2004; McKay et al. 2004).

The data reduction pipeline is built-up in modules which in combination lead to fully reduced spectra but permit the extraction of intermediate results when required by the user. Errors are propagated throughout the whole reduction chain (see Horrobin et al. 2008). The most important modules are described below:

- xsh_mbias and xsh_mdark combine series of raw biases and darks into a master bias and a master dark respectively. These steps also update a reference master bad pixel map;
- xsh_predict takes as input a single pinhole arc calibration frame (named format check, see left hand panel in Fig. 7) and computes a first guess for the wavelength solution and position of the center of each order taking into account information on atmospheric pressure and instrument temperature available in the FITS header;
- xsh_orderpos takes as input a continuum lamp illuminated single pinhole calibration frame (named order definition frame, see central panel in Fig. 7) and accurately traces the center of each order;
- xsh_mflat combines a series of raw flat field frames into a master flat field. It also traces the edge of each orders. In case of IFU calibrations, it traces the edge of each slitlet;
- xsh_2dmap takes as input a 9-pinhole mask arc frame (see an example in Fig. 7, right hand panel) together with a first guess wavelength solution derived by the preceding recipes and determines the wavelength and spatial scale calibration. Two calibration methods are proposed: either a classical method based on two dimensional polynomial fitting of the detected arc lines or a method based on the optimization of a physical model of the instrument (see Bristow et al. 2008);
- xsh_flexcomp updates the wavelength solution to correct for the effect of flexures and temperature drifts using the first frame of the active flexure compensation sequence taken during each pointing (see Sect. 3.5.2);
- xsh_response takes as input observations of a spectrophotometric standard star and computes the response function;
- xsh_scired_slit_stare, xsh_scired_slit_nod and xsh_scired_slit_onoff recipes process science data for the three main observing strategies used in slit mode: staring, nodding along the slit and sampling of the sky off target, respectively. These recipes first subtract the bias (UVB and VIS) or the master dark (NIR) and divide by a master flat-field. When less than three science frames per pointing are given as input, cosmic ray rejection using laplacien edge detection method described in van Dokkum (2001) is applied to each frame, otherwise frames are combined with a Kappa-Sigma clipping. In the staring case, the sky background is fitted and subtracted taking advantage of the fine sampling naturally provided by distortions of the spectral format following prescriptions detailed in Kelson (2003). In case of nodding along the slit, the so-called double pass sky subtraction is applied (first pass: subtraction of frames from the second position from those of the first one to produce a difference

[1] Available at http://www.eso.org/sci/software/pipelines/
[2] Available at http://www.eso.org/sci/software/cpl/esorex.html
[3] Available at http://www.eso.org/sci/software/gasgano/

Table 2. Detector performances.

Chanel	UVB	VIS	NIR
Detector type	e2v CCD44-82	MIT/LL CCID 20	Hawaii 2RG (substrate removed)
QE	80% at 320 nm 88% at 400 nm 83% at 500 nm 81% at 540 nm	78% at 550 nm 91% at 700 nm 74% at 900 nm 23% at 1000 nm	85%
Gain (e^-/ADU)	High: 0.62 Low: 1.75	High 0.595 Low: 1.4	2.12
Readout noise (e^- rms)	Slow: 2.5 Fast: 4.5	Slow 3.1 Fast: 5.2	Short DIT: ~25 DIT > 300 s: ~8
Full frame readout time (s)	1 × 1, slow-fast: 70–19 1 × 2, slow-fast: 38–12 2 × 2, slow-fast: 22–8	1 × 1, slow-fast: 92–24 1 × 2, slow-fast: 48–14 2 × 2, slow-fast: 27–9	0.665 (for a single readout)
Dark current (e^-/pix/h)	< 0.2	<1.1	21
Fringing amplitude		~5% peak-to-valley	
Non-linearity	Slow: 0.4% Fast: 1.0%	Slow: 0.8% Fast: 0.8%	<1% up to 45 000 ADU

frame; second pass: co-addition of the difference frame with a negative and shifted version of itself to co-add signal from the two positions and remove residuals due to variations in the sky background). These recipes produce, for each arm, a two-dimensional rectified spectrum that is wavelength, spatial scale and flux calibrated. It is possible to automatically detect objects and extract one-dimensional spectra with either a simple sum over an aperture or an optimal extraction;

– xsh_scired_ifu_stare and xsh_scired_ifu_onoff process IFU data and reconstruct calibrated data cubes for each arm. These recipes are similar to their slit mode equivalents described above. The flat-fielding step corrects for the difference in throughput between the two lateral sub-fields and the central one (see Sect. 2.2.3). Note that due to the small field of view of the IFU, nodding within the IFU is not a recommended observing strategy and thus is not supported by the pipeline.

3. X-shooter performance

3.1. Detectors

The performance of the detectors of each arm are given in Table 2 for all readout modes offered for science observations and calibrations.

3.2. Spectral format

The spectral format of X-shooter is fixed. The whole spectral range is covered by 12 orders in the UVB, 15 in the VIS, and 16 in the NIR. Orders are strongly curved (parabolic) and the spectral line tilt varies along the orders. Both slit height and width projection also vary from order to order and along each order due to a variable anamorphic effect introduced by the prisms (crossed twice). The minimum separation between orders is ~4 (unbinned) pixels to allow inter-order background evaluation. The dichroic crossover between UVB-VIS and VIS-NIR is at 559.5 nm and 1024 nm respectively, near the location of atmospheric features. Grating line densities were chosen to have the crossovers occur near the ends of the order. The spectral ranges on the detector and blaze wavelength for each order are given in Table 3 together with an example of a Th-Ar slit frame for each arm. These measurements are in excellent agreement with the predicted spectral format (Spanò et al. 2006).

3.3. Image quality and spectral resolution

In terms of image quality, spectral resolution and sampling, the three arms of X-shooter perform fully within specifications[4]. Resolution and sampling as a function of slit width are given in Table 4.

3.4. Efficiency

Thanks to the very high efficiency of the two dichroics splitting light between the three arms (see Fig. 4) and the careful optimization of each arm, the resulting overall throughput of X-shooter is very high. The efficiency for each order as measured during the last commissioning run using spectro-photometric standard BD+17 4708 is given in Fig. 8. Taking orders individually (i.e. not combining signal from adjacent orders), the total efficiency (including telescope and detectors) peaks at 33%, 34% and 31% for the UVB, VIS and NIR arm, respectively.

The overall efficiency is essentially as predicted by multiplying efficiencies of the different optical elements and detectors except for the J-band where it is ~30% below our predictions, due to losses that can only be partly explained by scattering in the ZnSe cross-disperser prisms.

[4] The original specifications for the resolution ($R = \lambda/\Delta\lambda$) with a 1″ slit were: $R > 5000$ for the UVB arm, $R > 7500$ for the VIS arm and $R > 4800$ for the NIR arm with a sampling of the line spread function >5 pixels. For a 0.6″ slit, the specifications were: $R > 7600$ for the UVB arm, $R > 11\,500$ for the VIS arm and $R > 7000$ for the NIR arm with a sampling of the line spread function >3 pixels.

Table 3. The X-shooter spectral format for the UVB (top), VIS (middle) and NIR (bottom) arm as measured at the telescope.

Order	Min. wavelength (nm)	Blaze wavelength (nm)	Max. wavelength (nm)	Example of a ThAr calibration frame
			UVB	
24	293.6	312.2	322.3	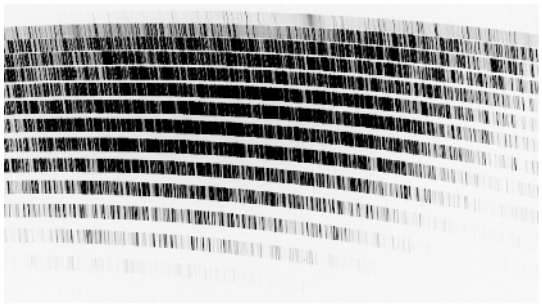
23	306.2	325.0	336.2	
22	320.0	339.8	351.4	
21	335.1	356.1	368.0	
20	351.8	373.5	386.2	
19	370.1	393.2	406.4	
18	390.6	414.5	428.9	
17	413.4	438.8	454.0	
16	439.1	466.4	482.2	
15	468.3	496.8	514.2	
14	501.6	531.0	550.8	
13	540.1	556.0	593.0	
			VIS	
30	525.3	550.5	561.0	
29	535.8	568.0	580.2	
28	554.6	585.9	600.8	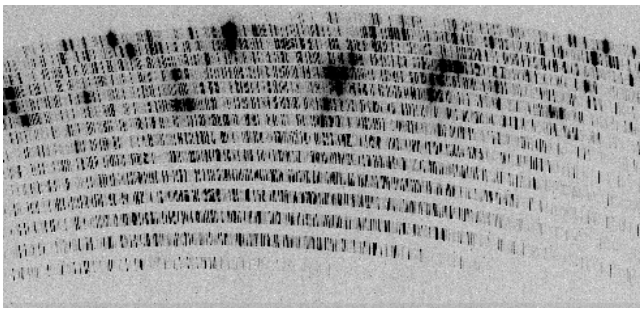
27	575.2	607.7	622.9	
26	597.4	629.5	646.8	
25	621.3	653.8	672.5	
24	647.2	682.1	700.4	
23	675.4	711.2	730.7	
22	706.1	742.6	763.8	
21	739.7	777.6	800.0	
20	777.0	815.8	839.8	
19	817.6	860.2	883.8	
18	862.9	904.3	932.7	
17	913.7	957.3	987.4	
16	970.7	1001.6	1048.9	
			NIR	
26	982.7	1005.8	1034.2	
25	1020.5	1046.0	1076.7	
24	1062.0	1089.6	1122.9	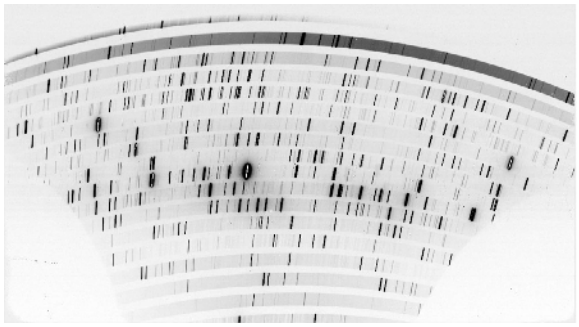
23	1106.6	1137.0	1173.1	
22	1155.2	1188.6	1228.0	
21	1208.2	1245.2	1288.5	
20	1266.5	1307.5	1355.2	
19	1330.3	1376.3	1429.4	
18	1400.8	1452.8	1511.5	
17	1479.5	1538.2	1604.0	
16	1567.1	1634.4	1708.7	
15	1667.8	1743.3	1823.3	
14	1785.7	1867.9	1952.8	
13	1922.6	2011.5	2102.0	
12	2082.9	2179.3	2275.6	
11	2272.3	2377.28	2480.7	

Notes. The minimum and maximum wavelength recorded on the detector together with the blaze wavelength are given for each order; on the right column, an example of wavelength calibration frame taken with a ThAr lamp for each arm.

Table 4. Measured resolution and sampling as a function of slit width.

	UVB			VIS			NIR	
Slit width (″)	Resolution ($\lambda/\delta\lambda$)	Sampling (pix/FWHM)	Slit width (″)	Resolution ($\lambda/\delta\lambda$)	Sampling (pix/FWHM)	Slit width (″)	Resolution ($\lambda/\delta\lambda$)	Sampling (pix/FWHM)
0.5	9100	3.5	0.4	17 400	3.0	0.4	11 300	2.0
0.8	6300	5.2	0.7	11 000	4.8	0.6	8100	2.8
1.0	5100	6.3	0.9	8800	6.0	0.9	5600	4.0
1.3	4000	8.1	1.2	6700	7.9	1.2	4300	5.3
1.6	3300	9.9	1.5	5400	9.7	1.5	3500	6.6
IFU	7900	4.1	IFU	12 600	4.2	IFU	8100	2.8

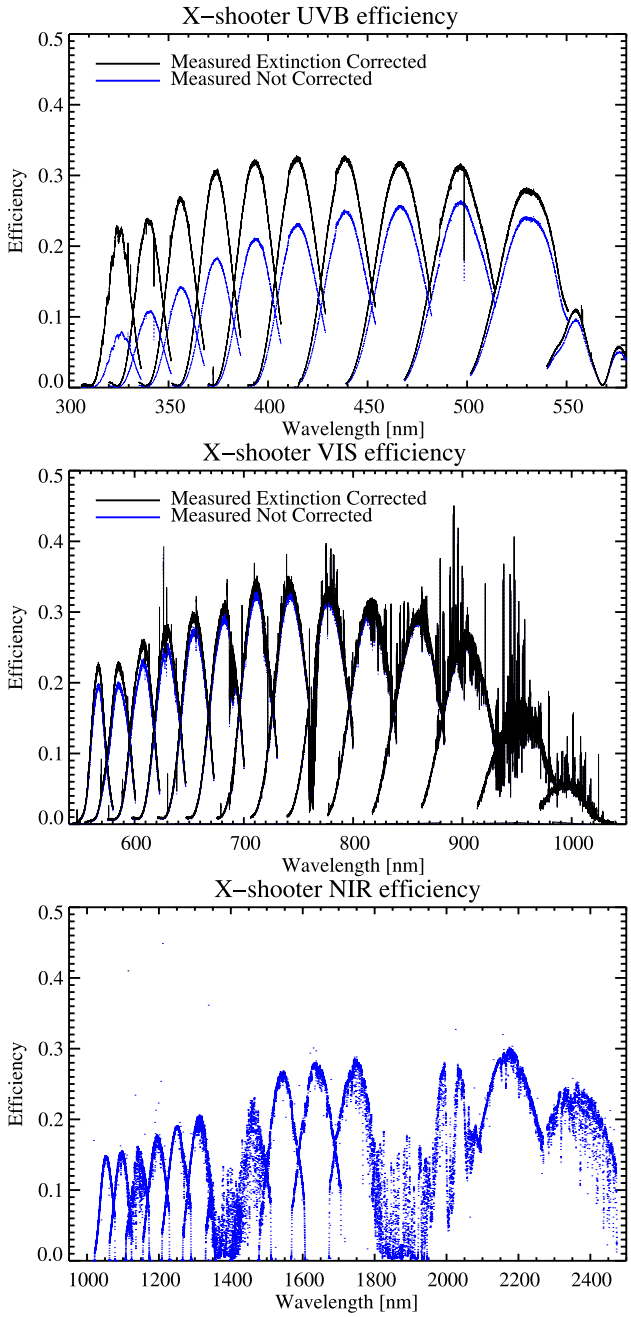

Fig. 8. The overall throughput of X-shooter, including telescope, as measured during the last commissioning run in september 2009 using spectro-photometric standard BD+17 4708. Blue curves represent raw measurements and black curves show the efficiency corrected for atmospheric extinction (UVB and VIS only).

3.5. Stability

Being mounted at the Cassegrain focus, X-shooter is subject to a changing gravity vector, hence instrument flexure has to be kept under control.

This splits into two components: (i) flexure within each spectrograph (i.e. after the slit) that mainly affects the quality of the wavelength calibration and the sky subtraction (see Sect. 3.5.1); (ii) flexure of the instrument backbone (i.e. before the slit) that affects the relative alignment of the three spectrographs (see Sect. 3.5.2).

3.5.1. Spectrograph flexures

Changes in the spectral format with position have been analyzed in detail during integration and testing in Garching and further checked during commissioning in Paranal. Performance at the telescope is shown in Fig. 9.

For the UVB and the VIS arm, the image motion measured throughout the whole detector using many calibration lines is identical, meaning that flexure induces a simple rigid shift of the spectral format. The amplitude of this displacement with respect to the position at zenith for a full rotation of the instrument at a zenith distance of 60° is $\lesssim$1.15 pixels in the UVB arm and $\lesssim$ 1.0 pixel in the VIS arm as shown in panel (a) and (b) of Fig. 9. No variation of image quality is measured for those two arms.

Concerning the NIR arm, the flexure behavior is more complex as illustrated in panel (c) of Fig. 9 which shows with different colors the recorded image motion for various calibration lines throughout the spectral format. Relative to their (x, y) position at zenith, spectral lines move by up to 1.4 pixels. However, this effect is larger on the edges than in the center of the detector hinting at an effect of flexure on image scale. This is possibly due to some small residual motion of the detector which is linked to a heavy copper bar reaching the LN2 tank to maintain its low operating temperature (see Sect. 2.5.4). This hypothesis is further supported by measured variations of the spot FWHM by up to ~15% (which, however, stays well within image quality specifications).

Note that the amplitude of the image motion discussed here is based on the extreme case of a full rotation of the instrument at 60° zenithal distance which never occurs during normal observations. In operation, these shifts are generally small and are not compensated mechanically (see Fig. 12).

3.5.2. Active flexure compensation of the backbone

One of the main challenges with the three arm design is to keep the three slits staring at the same patch of sky at any position angle and zenith distance. In order to always guarantee an alignment to better than 1/10th of the narrowest slit width, X-shooter is equipped with an active flexure compensation (AFC) system: each arm has a piezo mounted folding mirror which is adjusted during each acquisition, immediately after the telescope and the instrument have reached their position for science observations. Flexure is measured via application of the follwing recipe:

1. take simultaneously in the 3 arms an arc spectrum through the 0.5″ pinhole located in the spectrograph slit slide/wheel (Fig. 10a);
2. take a spectrum using a reference 0.5″ pinhole in the cassegrain focal plane (see Fig. 10b);
3. measure the displacement between the two frames (at the undeviated wavelength of the atmospheric dispersion compensator) using a cross-correlation algorithm;
4. send corresponding commands to piezos (Fig. 10c);
5. repeat steps 2 & 3 to check convergence.

This whole procedure comes at no expenses in terms of overheads since it is done in parallel with the telescope active optics setup. It is operationally very robust and does not require any user interaction. Our measurements show that it reliably maintains the alignment of the three slits to better than 0.02″, as illustrated in Fig. 11. As a side product, the first frame of the sequence is actually an “attached” wavelength calibration that is used by the data reduction pipeline to correct the

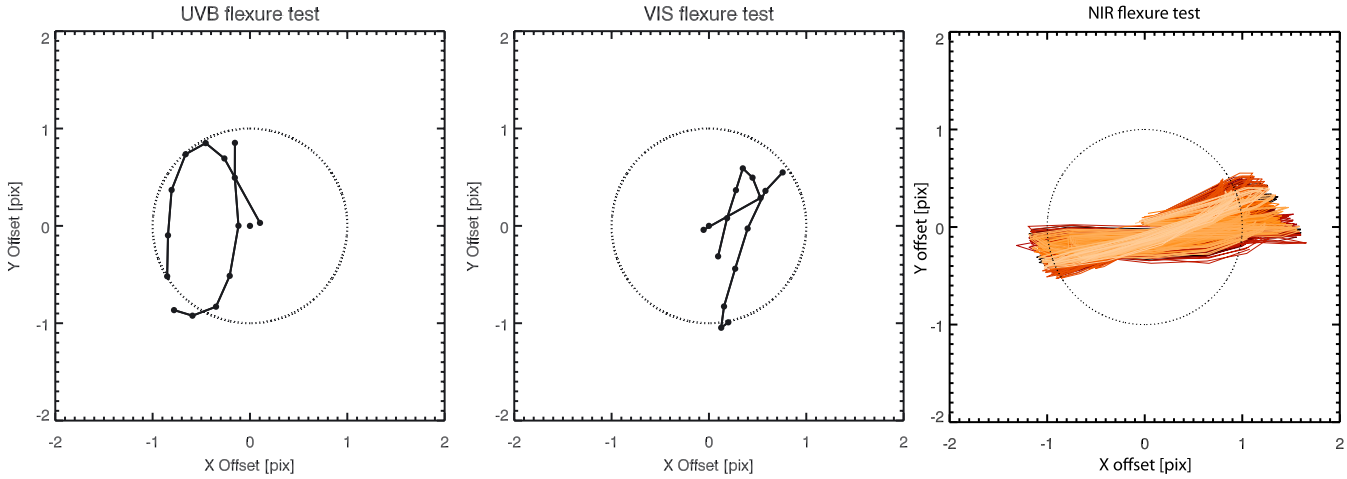

(a) UVB (b) VIS (c) NIR

Fig. 9. Measured image position for a full rotation of the instrument at a zenith distance of 60° taking as a reference (0, 0) the position measured at zenith. *X* and *Y* scales are in pixels. Pixel scale is ∼0.15″/pix for UVB and VIS, and ∼0.2″/pix for the NIR arm. The dotted circle shows limits set by our flexure specifications: ±1 pixel from zenith position. In panels **a)** and **b)**, corresponding to the UVB and the VIS arm, the curve shows the global motion of the spectral format obtained by averaging measurements obtained with five bright calibration lines. In panel **c)** corresponding to the NIR arm, the track followed by many individual calibration lines during the rotation of the instrument is shown.

wavelength solution for for thermally- and gravity-induced drifts (see Modigliani et al. 2010).

3.6. Near-IR arm background

The near-infrared sky is very dark in between the OH sky emission lines (Maihara et al. 1993). In order to reach sky background limited conditions, keeping the instrument background at the lowest possible level is therefore of utmost importance. Though a critical aspect of the performance of any near-IR spectrograph, it is however quite challenging and requires rigorous design and careful manufacturing (e.g. good baffling, limited number of cable feed-throughs).

The near-IR arm of X-shooter is a remarkably dark instrument: with a closed slit the measured background is below 0.01 e^-/s/pix. This means that assuming a sky background level as measured by Maihara et al. (1993), the instrument background should be a factor two to three below the sky. In addition, in an exposure of 1800 s, the photon noise from the instrument background would be around 4 e^- i.e. less than the read noise of the detector.

However, on sky measurements have revealed a background level estimated from the intensity of the inter-order space in the *J*- and the *H*-band a factor of three to five higher than the sky level. This stray light flux level rises in proportion to the slit width. A complete analysis of the background level using all commissioning data spaning a range of observing conditions further showed that this spurious background is correlated with ambient temperature as shown in Fig. 13. This indicates that it is probably caused by *K*-band radiation that is reflected by the detector into the camera and then comes back to the detector as a diffuse stray light background.

The immediate consequence is that in the *J*- and *H*-band the instrument in its present state is clearly not sky background limited.

4. Overview and future upgrades

In this paper, we have presented key figures demonstrating X-shooter's high performance on sky. This unique instrument lives up to expectations in terms of high throughput, resolution and exquisite image quality. It is overall a bit less stable than originally targeted but flexures are nevertheless kept within a very reasonable range ensuring no significant impact on science performance. The novel concept developed to compensate for backbone flexures and accurately maintain the three slits staring at the same patch of sky is very efficient and robust in operations.

After two "science verification" runs[5] in August and September 2009, the instrument started regular operation in period 84, that is on October 1st, 2009. In the first four calls for proposals for the VLT in which X-shooter has been offered (ESO Period 84 to 87), it has been the second most requested of the 14 available instruments, with a ratio requested versus scheduled observing time of 3.2. The first year of operations confirms the high versatility of the instrument and the very broad range of topics tackled by X-shooter, as anticipated in the original science case analysis, from stellar astrophysics (see e.g. Bragaglia et al. 2010; Schwope & Christensen 2010; Rigliaco et al. 2011; Kaper et al. 2011), cosmic explosions (e.g. de Ugarte Postigo et al. 2010; D'Elia et al. 2010) to the high redshift Universe (e.g. Dessauges-Zavadsky et al. 2010; Fynbo et al. 2010; Christensen et al. 2010).

Several ideas to further improve the performance of X-shooter or add new functionalities have been proposed. The most advanced one concerns the reduction of the *J*- and *H*-band background. As explained in Sect. 3.6, due to scattered light from the very bright thermal background dominated *K*-band orders, sky limited observations in the *J*- and *H*-band are currently not possible. There was a choice of either simply baffling the longest wavelength orders or placing a cold filter in front of some

[5] All science verification proposals and data are publicly available at http://www.eso.org/sci/activities/vltsv/xshootersv.html

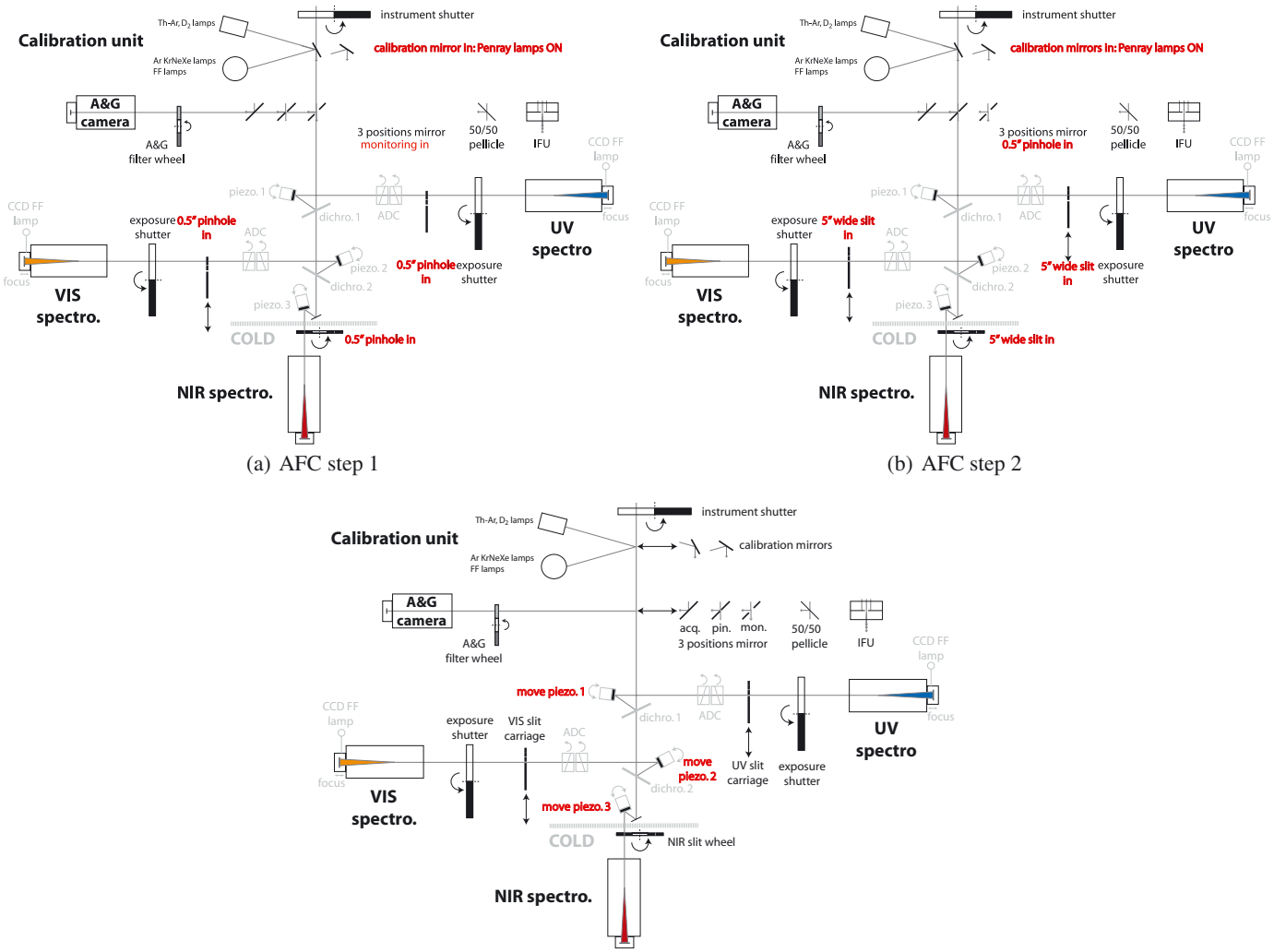

(a) AFC step 1 (b) AFC step 2

(c) AFC step 3

Fig. 10. The three steps of the flexure compensation procedure. For each step, functions that are moved are highlighted in red. In step 1, panel **a)**, the ArHgNeXe calibration lamps are switched on, the 3-position mirror in the A&G slide is set to the wide slot position and the 0.5″ pinhole is inserted in the slit unit of each spectrograph; in step 2, panel **b)**, the calibration lamp is still on, the 3-position mirror is set to the 0.5″ pinhole position and the wide 5″ slit is inserted in each slit unit; in step 3, panel **c)**, the piezo mounted folding mirrors are moved according to the measurements obtained in step 1 and 2.

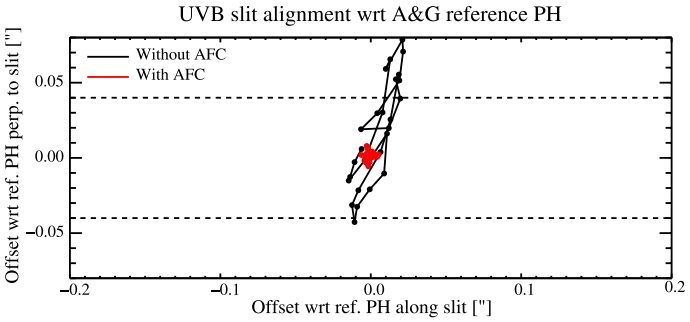

Fig. 11. Alignment of the UVB arm 0.5″ pinhole with respect to the focal plane reference pinhole with (red) and without the flexure compensation (black) through a full rotation of X-shooter at a zenith distance of 60°. The AFC allows to maintain the alignment to ∼0.01″, well within specification of 1/10th of the narrowest slit width.

of the slits. The second option was chosen and two new slits (0.6″ and 0.9″ wide) equipped with a short pass filter blocking the spectral range above 2 μm will be fitted into the NIR spectrograph slit wheel. Blocking the *K*-band radiation should restore the expected low background at the expense of the spectral range for those two new slits. In order to allow the acquisition of faint red sources – critical in the case of some GRB observations for instance –, the feasibility of adding a near-IR channel to the acquisition system is being investigated. In addition, the possibility to add spectro-polarimetric capabilities and the idea of replacing the piezo mounts of the folding mirrors to allow (counter)nodding in the UVB and VIS arms (i.e. nodding along the slit in the NIR arm while keeping the target at the same position in the UVB and VIS arm) have also been proposed.

5. The spectrum of the QSO B1422+231

Finally, as an example of the observing capability of the instrument, we show in Fig. 14 the reduced X-shooter spectrum of B1422+231 (z = 3.62). This QSO is sufficiently bright (V ∼ 16.5 mag) due to gravitational lensing to be observed at

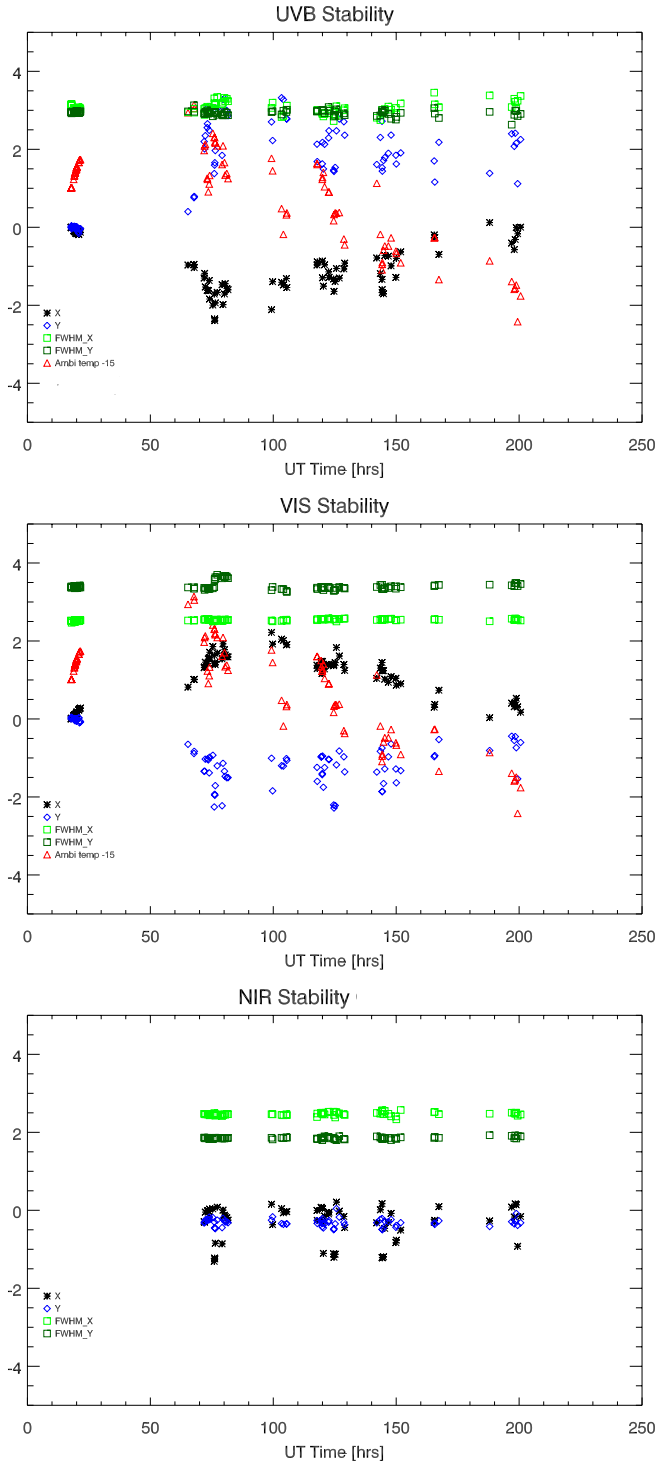

Fig. 12. Stability of the UVB (*top*), VIS (*center*) and NIR (*bottom*) spectrographs over 6 consecutive nights as measured during the third commissioning run. The dark and light green points show the FWHM in X and Y of a 0.5″ pinhole, the black and blue points show the X and Y position of a reference calibration line with respect to its position measured at zenith on the first day and the red points show the ambient temperature (for UVB and VIS only since it is irrelevant for the temperature controlled NIR arm).

medium-high resolution with high signal-to-noise in about 1 h. These data were obtained during the commissioning of the instrument in its full configuration in March 2009 to secure a template spectrum of a QSO over the full spectral range. The

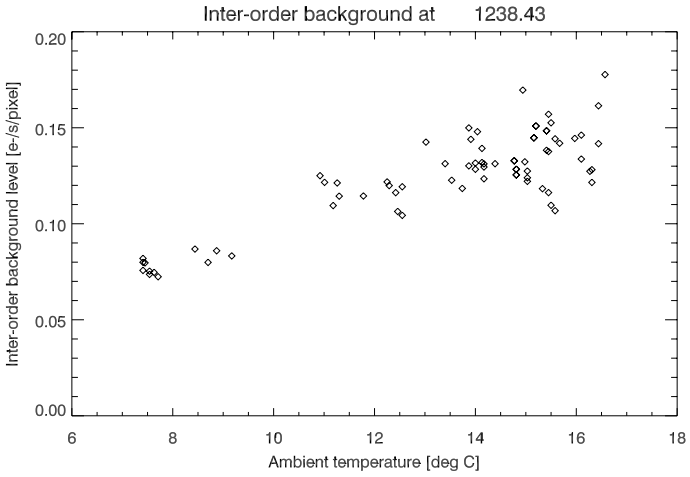

Fig. 13. Background level measured in the inter-order background region on both sides of order 21 at 1238.64 nm versus ambient temperature.

spectrum covers the wavelength interval 70−520 nm in the rest frame of the QSO. The integration time was 4800 s split over 4 × 1200 s exposures. The brightest two of the lensed QSO images, separated by 0.5″, were aligned along the slit and the extracted spectrum refers to the sum of the two. The reduction was carried out with the standard X-shooter data reduction package. The final signal-to-noise ratio is between 50 and 100 over most of the spectrum. The spectral resolution is 6200, 11000 and 8100 in the UVB, VIS and NIR spectral instrument arms respectively (on average two pixel sampling of the resolution element). The wavelength scale is calibrated to an accuracy of better than 2 km s^{-1} in the VIS arm and better than 4 km s^{-1} in the UVB and NIR arms, as verified on sky emission lines. The spectrum shown in Fig. 14 has been corrected for relative spectral response of the instrument via a standard star to a 5% accuracy. Since the night was not photometric, an accurate absolute flux scale could not be established.

The quality of the X-shooter spectra can be also judged from a comparison with the best high resolution data of this QSO in the literature. Songaila & Cowie (1996) discuss the metal absorption systems in the line of sight to this QSO from Keck HIRES spectra at resolution 36000 (total exposure time 8.3 h). Figure 15 shows two C IV metal systems for which the corresponding Lyα and Lyβ are also observed in the same exposure. A comparison with the corresponding tracings in Fig. 2 of Songaila & Cowie (1996) shows that all the components of the metal systems are detected although the resolution of the X-shooter is nominally a factor of 3 lower and the exposure time a factor of 4 shorter.

This is the first time that a QSO is observed over such a wide spectral range in a single observation. With a standard optical or infrared spectrograph only limited regions of the spectrum could be studied with a single exposure, with the potential risk of introducing errors in the final compilation of data taken at different times and under different weather conditions. With X-shooter data it is now possible to circumvent these obstacles.

Acknowledgements. The X-shooter project acknowledges financial support from the EU Descartes prize 2002 "Solving the gamma-ray burst riddle: the universe's biggest explosions" (PI Ed van den Heuvel), the Carlsberg foundation, the Netherlands Research School for Astronomy NOVA, and The Netherlands Organization for Scientific Research NWO. The design and implementation of the control software of X-shooter was carried out in the framework of a PRIN project of the MIUR (Italian Ministry of Education, University and Research).

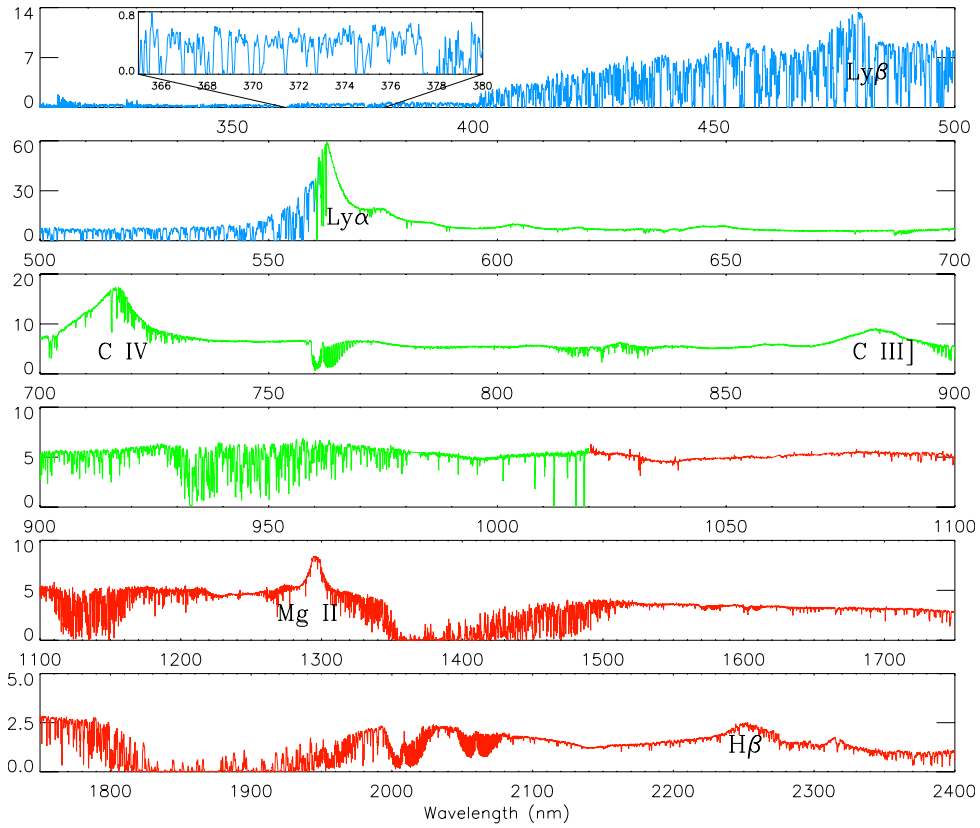

Fig. 14. Spectrum of the lensed QSO B1422+231. The blue part of the spectrum shows the UVB, the green the VIS, and the red the NIR data. No correction for telluric lines has been applied.

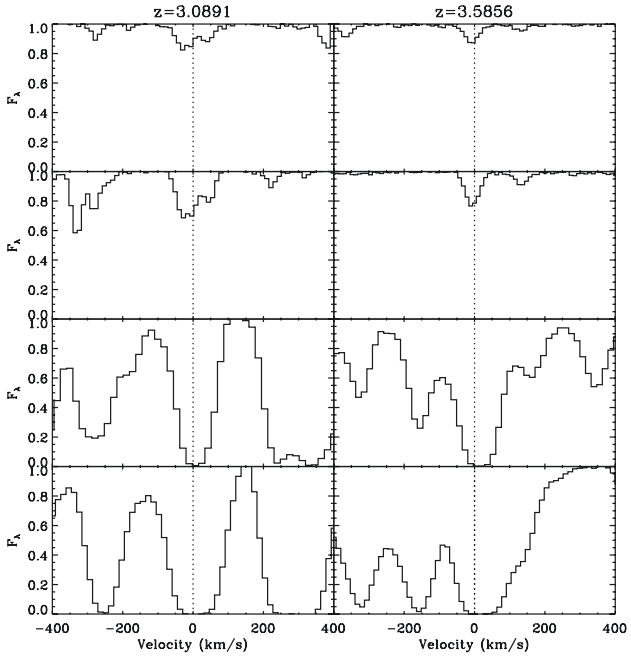

Fig. 15. The C IV λ1548 Å and the C IV λ1550 Å (*top*) lines of two high redshift metal systems in the line of sight to the QSO B1422+231 are shown in these normalized plots together with the corresponding Lyα and Lyβ absorptions. The data compare well with the observations of these systems with HIRES at Keck at three times the resolving power and from longer integration times published by Songaila & Cowie (1996). With the X-shooter, it was possible to observe all of these lines in parallel exposures within the blue and visual arm. The corresponding Mg II absorptions of the same systems fall in the NIR arm of the instrument.

We thank J. Prochaska for discussions on the optimal approach to the data reduction in the early phases of the project.

References

Banse, K., Ballester, P., Izzo, C., et al. 2004, in Astronomical Data Analysis Software and Systems (ADASS) XIII, ed. F. Ochsenbein, M. G. Allen, & D. Egret, ASP Conf. Ser., 314, 392
Beletic, J. W., Gerdes, R., & Duvarney, R. C. 1998, in Optical Detectors for Astronomy, ed. J. Beletic, & P. Amico, Astrophys. Space Sci. Lib., 228, 103
Bragaglia, A., Carretta, E., Gratton, R. G., et al. 2010, ApJ, 720, L41
Bristow, P., Kerber, F., Rosa, M. R., et al. 2008, SPIE Conf. Ser., 7014, 70143X
Christensen, L., D'Odorico, S., Pettini, M., et al. 2010, MNRAS, 406, 2616
de Ugarte Postigo, A., Goldoni, P., Thöne, C. C., et al. 2010, A&A, 513, A42
Delabre, B., Dekker, H., D'Odorico, S., & Merkle, F. 1989, SPIE Conf. Ser., 1055, 340
D'Elia, V., Fynbo, J. P. U., Covino, S., et al. 2010, A&A, 523, A36
Dessauges-Zavadsky, M., D'Odorico, S., Schaerer, D., et al. 2010, A&A, 510, A26
D'Odorico, S., Andersen, M. I., Conconi, P., et al. 2004, SPIE Conf. Ser., 5492, 220
D'Odorico, S., Dekker, H., Mazzoleni, R., et al. 2006, SPIE Conf. Ser., 6269, 626933
Finger, G., Dorn, R. J., Eschbaumer, S., et al. 2008, SPIE Conf. Ser., 7021, 70210P
Fynbo, J. P. U., Laursen, P., Ledoux, C., et al. 2010, MNRAS, 408, 2128
Goldoni, P., Royer, F., François, P., et al. 2006, SPIE Conf. Ser., 6269, 62692K
Guinouard, I., Horville, D., Puech, M., et al. 2006, in SPIE Conf. Ser., 6273, 62733R
Horrobin, M., Goldoni, P., Royer, F., et al. 2008, in 2007 ESO Instrument Calibration Workshop, ed. A. Kaufer, & F. Kerber, 221
Kaper, L., Ellerbroek, L. E., Ochsendorf, B. B., & Caballero Pouroutidou, R. N. 2011, Astron. Nachr., 332, 232
Kelson, D. 2003, PASP, 115, 688
Kerber, F., Saitta, F., Bristow, P., & Vernet, J. 2008, SPIE Conf. Ser., 7014, 70143Y
Maihara, T., Iwamuro, F., Yamashita, T., et al. 1993, PASP, 105, 940
McKay, D. J., Ballester, P., Banse, K., et al. 2004, SPIE Conf. Ser., 5493, 444

Meyer, M., Finger, G., Mehrgan, H., Nicolini, G., & Stegmeier, J. 1998, in SPIE Conf. Ser. 3354, ed. A. M. Fowler, 134
Modigliani, A., Goldoni, P., Royer, F., et al. 2010, SPIE Conf. Ser., 7737, 773728
Navarro, R., Elswijk, E., de Haan, M., et al. 2006, SPIE Conf. Ser., 6273, 62733O
Navarro, R., Elswijk, E., Tromp, N., et al. 2008, SPIE Conf. Ser., 7014, 70141Y
Raffi, G., & Wirenstrand, K. 1997, in SPIE Conf. Ser. 2871, ed. A. L. Ardeberg, 996
Rasmussen, P. K., Zerbi, F. M., Dekker, H., et al. 2008, SPIE Conf. Ser., 7014, 70143Z
Rigliaco, E., Natta, A., Randich, S., et al. 2011, A&A, 526, L6
Roelfsema, R., Albers, P., Lizon, J., et al. 2008, SPIE Conf. Ser., 7017, 701717
Saitta, F., Kerber, F., Bristow, P., et al. 2008, in 2007 ESO Instrument Calibration Workshop, ed. A. Kaufer, & F. Kerber, 57
Schwope, A. D., & Christensen, L. 2010, A&A, 514, A89
Songaila, A., & Cowie, L. L. 1996, AJ, 112, 335
Spanò, P., Delabre, B., Norup Sørensen, A., et al. 2006, SPIE Conf. Ser., 6269, 62692
van Dokkum, P. G. 2001, PASP, 113, 1420
Vernet, J., D'Odorico, S., Christensen, L., et al. 2009, The Messenger, 138, 4
Vidali, M., Di Marcantonio, P., Santin, P., Vernet, J., & Zacchei, A. 2006, SPIE Conf. Ser., 6274, 62740L

[1] European Southern Observatory, Karl Schwarzschild Strasse 2, 85748 Garching bei München, Germany
e-mail: jvernet@eso.org
[2] Astronomical Institute Anton Pannekoek, University of Amsterdam, Kruislaan 403, 1098 SJ Amsterdam, The Netherlands
[3] Niels Bohr Institute, Juliane Maries Vej 30, 2100 Copenhagen, Denmark
[4] GEPI – Observatoire de Paris, 5 place Jules Janssen, 92195 Meudon, France
[5] INAF – Osservatorio Astrofisico di Arcetri, Largo E. Fermi 5, 50125 Firenze, Italia
[6] INAF – Osservatorio Astronomico di Brera, via E. Bianchi 46, 23807 Merate, Italy
[7] Radboud Univ. Nijmegen, Postbus 9010, 6500 GL Nijmegen, The Netherlands
[8] ASTRON, Oude Hoogeveensedijk 4, 7991 PD Dwingeloo, The Netherands
[9] Laboratoire Astroparticule et Cosmologie, 10 rue A. Domon et L. Duquet, 75205 Paris Cedex 13, France
[10] European Southern Observatory, Alonso de Córdova 3107 Vitacura, Casilla 19001, Santiago de Chile 19, Chile
[11] Excellence Universe Cluster, Technische Universität München, Bolzmannstr. 2, 85748 Garching bei München, Germany
[12] INAF – Osservatorio Astronomico di Capodimonte, Salita Moiariello 16, 80131 Napoli, Italy
[13] INAF – Osservatorio Astronomico di Trieste, via Tiepolo 11, 34143 Trieste, Italy
[14] Physikalisches Institut Universität zu Köln, Zülpicher Strasse 77, 50937 Köln, Germany
[15] DTU Space, Juliane Maries vej 30, 2100 Copenhagen, Denmark
[16] Technologie Centrum FNWI, Science Park 904, 1098 XH Amsterdam, The Netherlands
[17] Space Telescope Science Institute, I3700 San Martin Drive, Baltimore, MD 21218, USA
[18] Laboratoire d'Astrophysique de Marseille, OAMP, Université Aix-Marseille & CNRS, 38, rue Frédéric Joliot Curie, 13388 Marseille Cedex 13, France
[19] Chester F. Carlson Center for Imaging Science, Rochester Institute of Technology, 54 Lomb Memorial Drive, 14623 Rochester, USA
[20] A.D.S. International S.r.l., via Roma 87, 23868 Valmadrera, Italy
[21] EC JRC Institute for Reference Materials and Measurements, 2440 Geel, Belgium